The Astrophysical Journal, 988:227 (15pp), 2025 August 1 https://doi.org/10.3847/1538-4357/ade70a

Commensal Transient Searches with MeerKAT in Gamma-Ray Burst and Supernova Fields

S. I. Chastain[1,2], A. J. van der Horst[2], A. Horesh[3], A. Rowlinson[4,5], A. Andersson[6], R. Diretse[7], M. Vaccari[7,8,9], R. P. Fender[6], and P. A. Woudt[10]
[1] Department of Physics and Astronomy, University of New Mexico, 210 Yale Blvd NE, Albuquerque, NM 87106, USA; sarchast@ttu.edu
[2] Department of Physics, George Washington University, 725 21st St NW, Washington, DC 20052, USA
[3] Racah Institute of Physics, The Hebrew University of Jerusalem, Jerusalem 91904, Israel
[4] Anton Pannekoek Institute for Astronomy, University of Amsterdam, Postbus 94249, 1090 GE Amsterdam, The Netherlands
[5] ASTRON, the Netherlands Institute for Radio Astronomy, Oude Hoogeveensedijk 4, 7991 PD, Dwingeloo, The Netherlands
[6] Astrophysics, Department of Physics, University of Oxford, Keble Road, Oxford OX1 3RH, UK
[7] Inter-University Institute for Data Intensive Astronomy, Department of Astronomy, University of Cape Town, 7701 Rondebosch, Cape Town, South Africa
[8] Inter-University Institute for Data Intensive Astronomy, Department of Physics and Astronomy, University of the Western Cape, 7535 Bellville, Cape Town, South Africa
[9] INAF—Istituto di Radioastronomia, via Gobetti 101, 40129 Bologna, Italy
[10] Department of Astronomy, University of Cape Town, Private Bag X3, Rondebosch 7701, South Africa
Received 2024 December 3; revised 2025 June 20; accepted 2025 June 21; published 2025 July 28

Abstract

The sensitivity and field of view of the MeerKAT radio telescope provide excellent opportunities for commensal transient searches. We carry out a commensal transient search in supernova and short gamma-ray burst fields using methodologies established by S. I. Chastain et al. We search for transients in MeerKAT L-band images with integration times of 30 minutes, finding 13 variable sources. We compare these sources to the VLASS and RACS survey data, and examine possible explanations for the variability. Additionally, for one of these sources we examine archival Chandra ACIS data. We find that 12 of these sources are consistent with variability due to interstellar scintillation. The remaining source could possibly have some intrinsic variability. We also split the MeerKAT L band into upper and lower halves, and search for transients in images with an integration time of 8 s. We find a source with a duration of 8–16 s that is highly polarized at the lowest frequencies. This source is spatially coincident with a star detected by the Transiting Exoplanet Survey Satellite. We conclude that this source may be consistent with a stellar flare. Finally, we calculate accurate upper and lower limits on the transient rate using transient simulations.

Unified Astronomy Thesaurus concepts: Radio continuum emission (1340); Radio transient sources (2008); Flare stars (540); Quasars (1319); Interstellar scintillation (855)

1. Introduction

With the establishment of new radio telescopes such as MeerKAT (J. L. Jonas 2009), ASKAP (S. Johnston et al. 2008), and LOFAR (M. P. van Haarlem et al. 2013), large areas of the sky are being imaged in a relatively short period of time. This has led to surveys such as the LOFAR Multi-frequency Snapshot Sky Survey (MSSS; A. J. Stewart et al. 2016), the LOFAR Two-meter Sky Survey (LoTSS; T. W. Shimwell et al. 2017), the ASKAP Variables and Slow Transients Survey (VAST; T. Murphy et al. 2021), the Rapid ASKAP Continuum Survey (RACS; D. McConnell et al. 2020), the Caltech–NRAO Stripe 82 Survey (CNSS; K. P. Mooley et al. 2016), and the Very Large Array Sky Survey (VLASS; M. Lacy et al. 2020). These surveys are finding a great variety of transients and variables on a wide range of timescales.

Gamma-ray burst (GRB) afterglows are transients that, at radio wavelengths, evolve on timescales of days up to years for the brightest events. J. K. Leung et al. (2021) searched for radio afterglows in RACS observations, finding a radio afterglow candidate for GRB 171205A. Tidal disruption events (TDEs) are another class of transient that is visible in radio and evolves on timescales of days to years. In the CNSS, M. M. Anderson et al. (2020) found a TDE. This was a very early finding that showed the promise of finding TDEs in large radio surveys. H. Dykaar et al. (2024) found 12 TDE candidates in the VAST Pilot Survey. A. Anumarlapudi et al. (2024) found a number of TDEs in the RACS survey, constraining detection rates, emission timescales, and the fraction of radio-bright TDEs. J. J. Somalwar et al. (2025) present a sample of TDEs detected and selected from VLASS radio observations. Two of these events that are particularly interesting are discussed by J. J. Somalwar et al. (2023). In VLASS, D. Z. Dong & G. Hallinan (2023) discovered a rare radio transient that would have been very difficult to find in targeted observations. B. D. Metzger et al. (2015) discuss the predicted transient rates for GRBs, TDEs, as well as supernovae (SNe) and potential magnetar emission in these surveys; as these surveys continue, this will be an interesting point of reference. All the aforementioned transients would historically be observed in targeted observations. However, since new radio surveys reobserve the same field multiple times over long timescales and have excellent sky coverage, they are enabling searches for populations of rare, bright transients that would normally require a large number of individual pointings that would result in many nondetections.

On shorter timescales of minutes to seconds, a number of new transients are being discovered, whose astrophysical origins are not yet well understood. A. J. Stewart et al. (2016)

found a nonrepeating transient in the MSSS with a duration of less than 11 minutes. A new, growing class of radio transients on these timescales are long-period repeating transients (LPRTs) with high linear polarization. M. Caleb et al. (2024) found a mode-switching transient with a period of 54 minutes within a target-of-opportunity observation of GRB 221009A. N. Hurley-Walker et al. (2023) discovered a radio transient with a period of 21 minutes as part of a program with the Murchison Widefield Array (S. J. Tingay et al. 2013) to monitor the Galactic plane. Recent observations of these transients have started to uncover their astrophysical origin. N. Hurley-Walker et al. (2024) report on a long-period radio transient with an optical counterpart corresponding to an M dwarf star. I. de Ruiter et al. (2025) associate one of these transients with an M dwarf–white dwarf binary system. These transient detections have been made in searches of images and have been enabled by the excellent instantaneous (u, v) coverage and sensitivity, and large field of view, of these new radio telescopes.

In addition to the aforementioned transients, commensal transient searches in MeerKAT data have yielded interesting results as well: the first MeerKAT transient was found in the same field as the black hole X-ray binary GX 339-4 (L. N. Driessen et al. 2020), along with several variable sources (L. N. Driessen et al. 2022); and several variables were found in the same field as the black hole X-ray binary MAXI J1820+070 (A. Rowlinson et al. 2022). In addition, S. I. Chastain et al. (2023) recently presented the results of commensal searches for transients on multiple timescales in eight short GRB fields. In this search, a large number of variables were found, of which 120 were variable due to interstellar scintillation and two showed possible intrinsic variability. All these sources were variable on timescales of days to months, and searches at shorter timescales of 15 minutes and 8 s did not result in significant transient detections. Interstellar scintillation is a phenomenon caused by the radio waves from a distant, typically compact source interacting with charged particles in the interstellar medium. This interaction causes the source to appear to dim and brighten. Interstellar scintillation can be informative about some of the properties of the interstellar medium and the size of the radio source.

In the study presented here, we perform commensal searches in fields of SNe and short GRBs observed by MeerKAT. These fields have been observed for 4–5 hr at a time, which allows for transient searches between different epochs but also at shorter timescales. We follow the methodology of S. I. Chastain et al. (2023), in particular the software and techniques established in that study, by making images with integration times of approximately 30 minutes. This allows us to probe the transient parameter space on timescales of hours, but also on timescales of days to years by comparing multiple observations of the same field. We also made images with integration times of 8 s of the full bandwidth, and of the lower and upper halves of the bandwidth. Given the large fractional bandwidth of the MeerKAT L band ($\Delta\nu/\nu \approx 0.6$), splitting up the band allows us to to potentially capture narrowband or steep-spectrum emission that would be missed by imaging the full bandwidth. Since the loss of sensitivity scales as approximately the square root of the bandwidth, the loss of sensitivity is not large compared to the potential scientific gain. Additionally, splitting the band allows for keeping data that would otherwise be affected by radio-frequency interference (RFI), since we can still have the other half of the band. In this paper, when it comes to the 8 s timescales, we will focus on the split-band images.

In Section 2, we describe the observations used in the survey and the data processing strategies. In Section 3, we describe the techniques and software used to find transient sources in the images. Then, in Section 4, we give an overview of the interesting sources that came out of our search. This is followed by Section 5, in which we discuss the possible counterparts and identification of the sources we find, along with the calculated transient rate as a result of this survey. In Section 6. we will look at the implications this survey has on future surveys and possible areas of improvement. Finally, in Section 7 we draw overall conclusions based on this study.

2. Observations

Deep observations were taken of short GRB and SN fields, and the sources in the center of the field were examined in detail by G. Schroeder et al. (2024), S. I. Chastain et al. (2024), and R. Ruiz-Carmona et al. (2025, in preparation). Each observation was approximately 4–5 hr in length, and the entire set of observations is summarized in Table 1. During the observations, the pointing of the telescope cycled between the target for approximately 15 minutes and a complex gain calibrator for about 5 minutes. In addition, a bandpass and flux calibrator were observed at either the beginning or end of the observations for approximately 10 minutes. These calibrators are also listed for each observation in Table 1.

Almost all observations were calibrated using version 2.0 of the ProcessMeerKAT pipeline, with the exception of the GRB 220730A observations, which were processed using version 1.1 of the pipeline (ProcessMeerKAT; J. D. Collier et al. 2021). As part of the calibration process, parts of the spectrum known to be heavily contaminated with RFI were flagged, as well as the edges of the bandpass, resulting in a bandwidth of approximately 800 MHz centered at 1.3 GHz, which is a reduction from 856 MHz in the raw data. The flagged frequency ranges differed slightly in some observations and can be over 50% of the MeerKAT L band, resulting in the variations in the center frequencies shown in Table 2. Calibration was performed in parallel over nine spectral windows (11 for ProcessMeerKAT 1.1). Common Astronomy Software Applications (The CASA TEAM et al. 2022) tools were used to perform complex gain and flux calibration, along with flagging for RFI, using the tasks *tfcrop* and *rflag*. After two rounds of calibration and flagging, the spectral windows were recombined into a single measurement set for imaging.

Imaging was performed using tclean, with parameters to account for non-coplanar baselines. The w-project gridder was used with 128 planes, the gain was set to 0.08, and multiterm multifrequency synthesis was used with two Taylor terms and scales of 0, 5, and 15. The imaging process started with a shallow image, using a threshold of 1 mJy. This image was used to create a model for phase self-calibration. Additional RFI flagging was performed using rflag. After self-calibration, images with an integration time of approximately 30 minutes were created by combining adjacent scans of 15 minutes into a single image. Primary beam correction was performed on the 30 minutes images using the katbeam library (M. S. de Villiers & W. D. Cotton 2022). The mean rms noise and the number of

Table 1
Observations Used in This Study, with the Start and End Times (in UT), Phase Center Position, Time Spent on the Target, and Calibrators Used

Name	Observation Start and End Time	R.A. (deg)	Decl. (deg)	Time (hr)	Bandpass	Complex Gain
SN 2019np	2019-01-11 23:15:47.5–2019-01-12 03:56:56.4	157.3415	29.5107	3.22	J1331+3030	J1120+1420
SN 2019np	2019-03-10 19:50:15.6–2019-03-11 00:13:8.9	157.3415	29.5107	2.97	J1331+3030	J1120+1420
SN 2019muj	2019-08-09 00:09:48.9–2019-08-09 05:08:41.4	36.5771	−9.8359	4.11	J0408-6545	J0240-2309
SN 2020ue	2020-01-14 01:43:23.7–2020-01-14 06:12:48.9	190.6949	2.6595	3.60	J1939-6342	J1256-0547
SN 2020ue	2020-01-19 23:14:52.5–2020-01-20 03:46:49.6	190.6949	2.6595	3.61	J1939-6342	J1256-0547
SN 2020ue	2020-02-06 00:55:23.8–2020-02-06 05:28:24.9	190.6949	2.6595	3.62	J1939-6342	J1256-0547
SN 2020hvf	2020-04-24 15:44:50.4–2020-04-24 21:22:13.9	170.3602	3.0147	4.98	J0408-6545	J1058+0133
SN 2020hvf	2020-05-01 17:15:5.2–2020-05-01 22:50:12.7	170.3602	3.0147	4.97	J0408-6545	J1058+0133
SN 2021smj	2021-07-10 12:45:57.1–2021-07-10 18:51:27.9	186.6940	8.8827	4.95	J0408-6545	J1150-0023
SN 2021smj	2021-07-23 11:50:54.9–2021-07-23 17:57:13.6	186.6940	8.8827	4.95	J0408-6545	J1150-0023
SN 2021qvv	2021-08-09 11:07:9.8–2021-08-09 15:48:2.6	187.0122	9.8056	3.96	J0408-6545	J1150-0023
SN 2021smj	2021-09-05 08:41:42.0–2021-09-05 14:48:8.7	186.6940	8.8827	4.95	J0408-6545	J1150-0023
SN 2022ffv	2022-03-31 09:22:5.0–2022-03-31 15:01:52.3	54.1238	−35.2893	4.97	J0408-6545	J0440-4333
SN 2022ffv	2022-04-01 09:29:45.1–2022-04-01 17:21:37.1	54.1238	−35.2893	4.97	J0408-6545	J0440-4333
SN 2022ffv	2022-04-14 08:22:1.1–2022-04-14 14:01:48.5	54.1238	−35.2893	4.98	J0408-6545	J0440-4333
GRB 220730A	2022-08-01 18:36:8.7–2022-08-01 22:40:46.5	225.0143	−69.4959	3.46	J1939-6342	J1619-8418
GRB 220730A	2022-08-03 16:30:46.1–2022-08-03 20:36:27.8	225.0143	−69.4959	3.47	J1939-6342	J1619-8418
GRB 220730A	2022-08-10 15:15:52.6–2022-08-10 19:22:14.4	225.0143	−69.4959	3.47	J1939-6342	J1619-8418
GRB 200522A	2022-08-16 23:22:42.4–2022-08-17 03:23:4.3	5.6820	−0.2832	3.47	J1939-6342	J0022+0014
GRB 200907B	2022-08-19 05:18:50.2–2022-08-19 09:23:44.0	89.0290	6.9062	3.47	J0408-6545	J0521+1638
GRB 210919A	2022-08-20 05:17:2.6–2022-08-20 09:19:8.5	80.2545	1.3115	3.46	J0408-6545	J0503+0203
GRB 210726A	2022-08-21 11:26:1.1–2022-08-21 15:29:43.0	193.2909	19.1875	3.46	J1331+3030	J1330+2509
GRB 200411A	2022-08-22 02:16:28.7–2022-08-22 06:03:30.9	47.6641	−52.3176	3.22	J0408-6545	J0210-5101
GRB 210323A	2022-08-23 20:17:47.4–2022-08-24 00:23:13.2	317.9461	25.3699	3.47	J1939-6342	J2236+2828
GRB 200219A	2022-08-24 00:47:39.5–2022-08-24 04:52:25.3	342.6385	−59.1196	3.46	J0408-6545	J2329-4730
GRB 220730A	2022-09-08 15:37:10.1–2022-09-08 19:42:19.8	225.0143	−69.4959	3.46	J1939-6342	J1619-8418
SN 2020eyj	2022-05-07 16:10:32.8–2022-05-07 21:05:17.3	167.9466	29.3893	3.96	J1120+1420	J0408-6545
SN 2020eyj	2022-10-28 04:47:5.0–2022-10-28 09:42:45.5	167.9466	29.3893	3.97	J1120+1420	J0408-6545

images for the timescale of 30 minutes are summarized in Table 3. The center frequency, number of images, and median rms noise for the 8 s images are summarized in Table 2. The 8 s images of the GRB 200522A field were not included due to artifacts from bright field sources.

3. Methods

We used the LOFAR Transients Pipeline (TRAP; J. D. Swinbank et al. 2015) for source-finding, source association, and image quality control. TRAP is also designed to calculate variability metrics based on source light curves, but we chose to do these calculations separately in order to account for a 10% systematic error. Quality control is taken care of in TRAP through multiple checks. The rms noise is measured in the inner part of the image by removing the brightest pixels. The measured noise in the image is compared to global allowed minimum and maximum values and put into a running histogram. After the first 100 images, if the noise is greater than 3σ from the mean, it is rejected. This resulted in the rejection of six images. There are other reasons why an image could have been rejected, such as beam shape, for which we relaxed the ellipticity requirements to a factor of 10, and with that, these six images were the only rejected ones.

Before determining variability, we only selected sources that were within $0.^{\circ}8$ of the center of the field. Given the fall-off of sensitivity and the complex shape of the beam, this restriction prevents effects on the flux of our sources in ways that are difficult to model accurately. Additionally, the noise within this distance to the center of the primary beam does not appreciably increase. In order to assess the variability of the sources, we use the variability measures V and η as defined by J. D. Swinbank et al. (2015), where I is the flux measurement of a source, ξ is the average flux weighted by the inverse of the flux measurement errors σ, and averages are indicated by bars above the quantities in these equations:

$$V_\nu = \frac{1}{\bar{I}_\nu}\sqrt{\frac{N}{N-1}(\bar{I}_\nu^2 - \bar{I}_\nu^2)} \quad (1)$$

$$\eta = \frac{1}{N-1}\sum_{i=1}^{N}\frac{(I_{\nu,i} - \xi_{I_\nu})^2}{\sigma_{\nu,i}^2}. \quad (2)$$

We recomputed V and η for every source found by TRAP, incorporating a 10% systematic error into the calculations of η, by adding it in quadrature to the flux errors reported by TRAP. For the 8 s images we took the additional step of computing an η value in 14 images at a time for each source and keeping the largest computed η value. This number of images was selected by testing the maximum number of images that can be used before a bright transient lasting 8 s or less gets washed out into an insignificant amount of variability. In other words, this step ensures that any short-timescale variation does not get averaged out over the large number of images included in the 8 s data set. For both the 8 s and 30 minutes images, we considered sources with $\eta > 2$ to be candidate variables. This value was chosen in our first study (S. I. Chastain et al. 2023) by examining a large number of sources and their variability. We also determined a signal-to-noise detection threshold in the

Table 2
Number of 8 s Images for Each Field, the Center Frequency, and the Median rms Noise

Target	Center Freq. (MHz)	No. of Images	Median rms Noise (μJy)
SN 2019np	1098	2799	318
SN 2019np	1498	2799	195
SN 2019muj	1098	1860	241
SN 2019muj	1498	1860	144
SN 2020ue	1098	4831	272
SN 2020ue	1498	4831	164
SN 2020hvf	1098	4489	262
SN 2020hvf	1498	4489	143
SN 2021smj	1098	6716	365
SN 2021smj	1498	6716	160
SN 2021qvv	1098	1792	523
SN 2021qvv	1498	1792	286
SN 2022ffv	1098	7611	482
SN 2022ffv	1498	7612	283
GRB 220730A	1030	6265	268
GRB 220730A	1480	6265	139
GRB 200907B	1030	1568	303
GRB 200907B	1480	1568	168
GRB 210919A	1030	1565	741
GRB 210919A	1480	1565	277
GRB 210726A	1030	1566	311
GRB 210726A	1480	1566	151
GRB 200411A	1030	1454	282
GRB 200411A	1480	1454	126
GRB 210323A	1030	1567	245
GRB 210323A	1480	1567	136
GRB 200219A	1030	1564	272
GRB 200219A	1480	1564	135
SN 2020eyj	1134	3573	353
SN 2020eyj	1498	3573	171

Table 3
Number of 30 minutes Images for Each Field and the Mean rms Noise

Target	No. of Images	Mean RMS Noise (μJy)
SN 2019np	12	31
SN 2019muj	12	31
SN 2020ue	33	37
SN 2020hvf	10	20
SN 2021smj	30	44
SN 2021qvv	8	77
SN 2022ffv	17	38
GRB 220730A	28	23
GRB 200522A	7	140
GRB 200907B	7	47
GRB 210919A	7	96
GRB 210726A	7	33
GRB 200411A	6	19
GRB 210323A	7	27
GRB 200219A	7	21
SN 2020eyj	16	36

same way as A. Rowlinson et al. (2022) and S. I. Chastain et al. (2023). We took a sample of 50% of the pixels that were included in the transient search and determined the threshold at which less than one false transient detection would occur by assuming the pixels follow a Gaussian distribution. Using this method, we determined a threshold of approximately 5.4 times the rms noise in the image for the 30 minutes images, and 6.4 times the rms noise in the image for the 8 s images. This threshold is only a rough approximation since the pixels do not follow a Gaussian distribution; see also the discussion by A. Rowlinson et al. (2022).

In order to reduce the number of sidelobes flagged as potential transients, we rejected all but the brightest source in a circular region of five beam widths around every source (measured by the beam's major axis), following S. I. Chastain et al. (2023). Some sidelobes still remained after this step, and we could have made this radius larger to attempt to catch more, but we did not want to risk losing any more potential candidates, so we removed these sidelobe sources in later steps by visual determination.

4. Results

4.1. 30 minutes Images

After performing the aforementioned steps to find transients, and then systematically reducing the number of spurious sources, we were left with 874 sources that had an η value greater than 2 or with a detection in only a single image. We made animations of these sources[11] to further categorize them. After visual examination, 289 sources were identified as sidelobes of brighter sources, 57 sources were due to noise patterns, 477 sources could not be categorized due to the lack of contrast in the visualization, 28 sources failed to make a proper animation due to only being detected in a single image, and 24 sources appeared to be astrophysical. Before remaking animations of the 477 sources that needed improved contrast, a forced fit was done at the locations of all of these sources in addition to the sources that were only detected in a single image and those that appeared to be astrophysical. This forced-fitting step was performed to ensure that any potential variables or transients were not due the effects of a source with low signal-to-noise ratio. After this step, only 52 sources remained with an η value above 2. Each of the 52 sources was examined, and sources that appeared to have variability due to issues with the image, such as an elliptical beam shape rotating over time to cause two sources to merge into one apparently bright source, or an extremely bright source causing issues across the image, were rejected, leaving 14 sources.

Out of these 14 sources, 11 showed variability on timescales longer than the observation length. Of the remaining three sources, the sources in the 30 minutes images show variability within the 4–5 hr observation, which could have been due to a bright source in the field. In order to determine whether this bright source was affecting these sources, we reran TRAP on the full observations, measuring the corrected η value for each of the three sources. After this step, the corrected η value for one of the sources was less than 2 and this source was removed from consideration. Therefore, our final count of variables in this data set is 13.

4.2. 8 s Images

In contrast to S. I. Chastain et al. (2023), we split the bandwidth of the MeerKAT L band in half in an attempt to increase the likelihood of capturing potential steep-spectrum or narrowband transients. We performed the same steps to find transients and remove spurious transients as in the 30 minutes

[11] Code available at https://github.com/dentalfloss1/sharedscripts as FindOutliers.py.

Table 4
Primary Beam-corrected Flux Measurements of Stokes *I* and *V* Flux of Source 96178 Using TRAP

Center Freq. (MHz)	Bandwidth (MHz)	$F_{\mathrm{int},I}$ (mJy)	$F_{\mathrm{int},V}$ (mJy)
989.0	200.0	1.93 ± 0.59	-1.44 ± 0.19
1207.1	200.0	1.18 ± 0.68	-0.43 ± 0.24
1388.9	200.0	1.03 ± 0.48	0.35 ± 0.16
1570.8	200.0	0.96 ± 0.57	0.05 ± 0.19

images, resulting in 1803 sources with η greater than 2. Movies were made of each source, and after removing sources that were either artifacts, likely satellites or other RFI, or had variability that seemed to be nonastrophysical in origin, we were left with one transient source.

This source, source 96178, is detected at an R.A. and decl. of ($317^\circ.565 \pm 0^\circ.003$, $25^\circ.397 \pm 0^\circ.003$) (J2000), and it has a duration of 8–16 s. It was initially only detected in the lower frequencies of the observing band in the GRB 210323A field. Upon detecting this transient, we recalibrated and reimaged the observation with the cross-hand polarizations included in order to obtain Stokes *V* polarization images. We found that the source seemed to have significant Stokes *V* polarization in the lowest frequencies. We additionally split the bandwidth into four instead of two parts and found the observed flux to be highest at the lowest frequencies. A summary of the measurements is given in Table 4. Similar to the 30 minutes images, the primary beam correction was then performed using the KATBEAM (M. S. de Villiers & W. D. Cotton 2022) library.

5. Discussion

5.1. Variable Sources

In the transient searches of the 30 minutes images, no transients were found, but we did identify 13 variable sources. These variable sources have already been verified to be of an astrophysical nature and not due to any calibration or statistical issues. In order to investigate the sources further, an initial search of the source positions was compared against catalogs contained in the Vizier (F. Ochsenbein et al. 2000) catalog access tool using a search radius of 2″ from the position of the variable source reported by TRAP. This initial search yielded an unrealistically large number of optical, infrared, and near-infrared counterparts. Therefore, we limited counterparts to those detected by the Transiting Exoplanet Survey Satellite (TESS; G. R. Ricker et al. 2015), X-ray catalogs, gamma-ray catalogs, and radio catalogs. See Section 5.2 for more information. From this search we find one possible X-ray counterpart to source 1278651 shown in Figure 1, for more details see Section 5.1.2. The RACS (D. McConnell et al. 2020) and VLASS (M. Lacy et al. 2020) survey data were also searched for counterparts to the variable sources. For some sources, catalog data were already available; for other sources, PySE (H. Spreeuw et al. 2018) was used to fit a source in the survey data at the location of the variable source. Cutouts from VLASS were obtained from Canadian Initiative for Radio Astronomy Data Analysis (CIRADA, cutouts.cirada.ca) while cutouts from RACS were obtained from the CSIRO Data Portal CASDA Cutout Service (https://data.csiro.au).

5.1.1. Sources with Radio Counterparts

All of our variable sources together with their counterpart measurements, or forced measurements, are shown in Tables 5 and 6. The light curves for these sources are shown in Figures 2–4.

Our measurements from MeerKAT at 1.3 GHz agree fairly well with the catalog measurements for most of these sources, with the exceptions being the two sources discussed specifically in this section. There is one notably bright source, source 1267266, which showed variability between the NVSS and FIRST surveys. The integrated flux was 10 mJy in NVSS and 7.2 mJy in FIRST. In Figure 2, we see this same range of variability in the MeerKAT data as well.

5.1.2. Source 1278651

Source 1278651 shows variability in RACS and VLASS, but the detections are only marginal. The measurements using PySE shown in Table 6 roughly fall within the range of our measurements at 1.3 GHz (see also Figure 3). This variability in the time between observations could be intrinsic, due to the signal-to-noise ratio, or due to scintillation as will be discussed in Section 5.3.

This source has conflicting multiwavelength catalog data: C. A. L. Bailer-Jones et al. (2021) show a star approximately 1.3 kpc away within 1″ of the source using Gaia (T. Prusti et al. 2016). However, there is also a faint X-ray source at this location: J. Liu (2011) detect a source with Chandra, reporting a distance of 12 Mpc, which is also present in the second Chandra Source Catalog (I. N. Evans et al. 2010). Since this was found in an extragalactic field and the variability is consistent with interstellar scintillation, these X-ray measurements hint at this source being an active galactic nucleus (AGN). In order to examine this source further, we downloaded archival Chandra ACIS (G. P. Garmire et al. 2003) data using the Chandra Interactive Analysis of Observations (CIAO; A. Fruscione et al. 2006) software tools. The data were reprocessed and merged into a single image, shown in Figure 1 along with an observation in which it was detected. Based on this image, the Chandra source does not appear to be confidently detected in the combined image. However, in one of the observations, the source is clearly detected. This source could possibly be variable in X-rays. The image was made from Chandra ObsId 4175, 4176, 3949, 2942, 17548, 17541, 17540, 16234, 16233, 16232, and 16231.

5.1.3. Source 1290071

Source 1290071 is notable for its lack of variability in RACS. Our measurements show this source varying between a lower flux of around 0.8 mJy and a higher flux state of around 1.2 mJy (see Figure 4). Notably, the RACS measurements at both 890 MHz and 1400 MHz are consistent with our higher flux measurements and stable in flux. However, these measurements do not necessarily rule out interstellar scintillation as the main cause of variability, due to the cadence of the RACS observations.

5.2. Other Multiwavelength Data and Classification

An initial search of the available optical catalogs with Vizier (F. Ochsenbein et al. 2000) revealed that, in addition to the

Table 5
Radio Catalog Counterparts for Variable Sources in Our MeerKAT Survey That are Visible to Both VLASS and RACS

Source	R.A.	Decl.	$F_{\rm int}$ (mJy)	F_{pk} (mJy)	Frequency (GHz)	Date	Survey	Measurement
1252675	157.3791	29.8533	2.5 ± 0.5	1.4 ± 0.2	2.7	2019-04-22 23:38:59	VLASS	Catalog
1252675	157.3791	29.8533	1.2 ± 0.5	1.1 ± 0.2	1.4	2021-01-03 19:03:30	RACS	PySE
1252675	157.3791	29.8533	1.3 ± 0.5	1.2 ± 0.3	1.4	2021-01-02 19:10:06	RACS	PySE
1252803	157.2391	29.9353	−0.04 ± 0.3	0.8 ± 4.0	2.7	2019-04-22 23:38:59	VLASS	PySE
1252803	157.2391	29.9353	−0.08 ± 0.2	0.07 ± 0.1	2.7	2021-12-03 9:39:52	VLASS	PySE
1252803	157.2391	29.9353	0.06 ± 0.3	−0.5 ± 0.2	1.4	2021-01-03 19:03:30	RACS	PySE
1252803	157.2391	29.9353	0.07 ± 0.4	−0.6 ± 2.0	1.4	2021-01-02 19:10:06	RACS	PySE
1260388	191.0687	2.334	1.6 ± 0.3	1.3 ± 0.1	2.7	2019-04-21 8:11:40	VLASS	Catalog
1260388	191.0687	2.334	1.7 ± 1.1	1.5 ± 0.5	0.89	2020-04-30 14:06:00	RACS	PySE
1260388	191.0687	2.334	1.7 ± 1.1	1.5 ± 0.5	0.89	2020-04-30 14:23:00	RACS	PySE
1260388	191.0687	2.334	1.7 ± 1.1	1.5 ± 0.5	0.89	2020-05-01 13:24:00	RACS	PySE
1260388	191.0687	2.334	1.7 ± 1.1	1.5 ± 0.5	0.89	2020-05-01 13:41:00	RACS	PySE
1260388	191.0687	2.334	1.4 ± 0.4	1.4 ± 0.2	1.4	2021-01-03 22:22:34	RACS	PySE
1260388	191.0687	2.334	1.3 ± 0.4	1.3 ± 0.2	1.4	2021-01-09 22:37:42	RACS	PySE
1260388	191.0687	2.334	1.4 ± 0.4	1.3 ± 0.2	1.4	2021-01-03 22:02:39	RACS	PySE
1260388	191.0687	2.334	1.3 ± 0.4	1.3 ± 0.2	1.4	2022-07-30 3:24:18	RACS	PySE
1260578	190.8379	2.4131	1.5 ± 0.3	1.2 ± 0.1	2.7	2019-04-21 8:11:58	VLASS	Catalog
1260578	190.8379	2.4131	−0.09 ± 0.7	1.8 ± 8.0	0.89	2020-04-30 14:06:00	RACS	PySE
1260578	190.8379	2.4131	−0.1 ± 0.7	1.1 ± 3.5	0.89	2020-04-30 14:23:00	RACS	PySE
1260578	190.8379	2.4131	−0.1 ± 0.7	1.5 ± 5.6	0.89	2020-05-01 13:24:00	RACS	PySE
1260578	190.8379	2.4131	−0.01 ± 0.7	1.6 ± 6.4	0.89	2020-05-01 13:41:00	RACS	PySE
1260578	190.8379	2.4131	0.7 ± 0.3	0.7 ± 0.2	1.4	2021-01-03 22:22:34	RACS	PySE
1260578	190.8379	2.4131	0.8 ± 0.3	0.7 ± 0.2	1.4	2021-01-03 22:02:39	RACS	PySE
1260578	190.8379	2.4131	0.6 ± 0.4	0.6 ± 0.2	1.4	2021-01-09 22:37:42	RACS	PySE
1260578	190.8379	2.4131	0.6 ± 0.4	0.5 ± 0.2	1.4	2021-01-09 22:17:57	RACS	PySE
1266989	170.58	2.8567	0.2 ± 0.3	−0.07 ± 0.09	2.7	2020-08-22 21:59:48	VLASS	PySE
1266989	170.58	2.8567	0.5 ± 0.2	0.4 ± 0.1	2.7	2023-02-02 12:06:59	VLASS	PySE
1266989	170.58	2.8567	0.5 ± 0.5	0.3 ± 0.2	0.89	2023-12-31 21:04	RACS	PySE
1266989	170.58	2.8567	0.5 ± 0.5	0.3 ± 0.2	0.89	2024-01-25 19:12	RACS	PySE
1266989	170.58	2.8567	−0.09 ± 0.3	0.2 ± 0.3	1.4	2021-01-16 20:45:26	RACS	PySE
1266989	170.58	2.8567	−0.08 ± 0.2	0.2 ± 0.4	1.4	2021-01-09 20:58:10	RACS	PySE
1267266	170.4347	2.8388	10.0 ± 0.5	…	1.4	1995-02-27	NVSS	Catalog
1267266	170.4347	2.8388	7.2	7.2	1.4	1998-07-01	FIRST	Catalog
1267266	170.4347	2.8388	6.1 ± 0.2	6.1 ± 0.2	2.7	2018-01-12 11:12:44	VLASS	PySE
1267266	170.4347	2.8388	8.8 ± 1.4	7.2 ± 0.4	0.89	2020-05-01 12:50:35	RACS	PySE
1267266	170.4347	2.8388	5.9 ± 0.3	5.9 ± 0.2	1.4	2021-01-09 20:58:10	RACS	PySE
1267266	170.4347	2.8388	5.6 ± 0.3	5.6 ± 0.2	1.4	2021-01-16 20:45:26	RACS	PySE
1267302	170.4211	3.3767	0.0 ± 0.3	3.2 ± 60.0	2.7	2020-08-22 21:39:45	VLASS	PySE
1267302	170.4211	3.3767	−0.02 ± 0.2	0.7 ± 3.6	2.7	2023-02-02 12:40:38	VLASS	PySE
1267302	170.4211	3.3767	0.1 ± 0.6	−0.7 ± 1.5	0.89	2020-05-01 12:50	RACS	PySE
1267302	170.4211	3.3767	0.1 ± 0.6	−0.7 ± 2.0	0.89	2020-05-01 13:07	RACS	PySE
1267302	170.4211	3.3767	−0.3 ± 0.3	−0.2 ± 0.1	1.4	2021-01-16 20:45:26	RACS	PySE

Note. When indicated, source measurements were made using PySE (H. Spreeuw et al. 2018) on image cutouts acquired from the Canadian Initiative for Radio Astronomy Data Analysis (CIRADA) and the CSIRO Data Portal CASDA Cutout Service. VLASS data are from Y. A. Gordon et al. (2021), NVSS data from J. J. Condon et al. (1998), FIRST data from D. J. Helfand et al. (2015), and RACS data from D. McConnell et al. (2020) and C. L. Hale et al. (2021).

aforementioned radio data, almost all of the variable sources, except for 1290071 and 1305970, have an optical counterpart within two arcseconds of the position of the variable source reported by TRAP. It is difficult, however, to confirm the association between the optical and radio sources. D. J. Helfand et al. (2015) discuss the challenge of confirming counterparts between relatively low-resolution radio telescopes and optical catalogs, a challenge that is only more difficult with deep optical catalogs. It is notable that the two sources that have no optical counterpart have low declinations where there are many fewer instruments and less catalog data with which to compare. While it is likely that at least some of these sources are scintillating AGNs, the coarse localization makes it difficult to confirm the true nature of these sources. Due to these aforementioned challenges, we only considered radio, X-ray, or gamma-ray sources due to the higher potential of association with a radio source, as well as TESS sources since they have light curves available to which we can compare time variability.

Table 6
Radio Counterparts for Variable Sources Continued from Table 5

Source	R.A.	Decl.	$F_{\rm int}$ (mJy)	F_{pk} (mJy)	Frequency (GHz)	Date	Survey	Measurement
1278651	54.8335	−35.8063	0.34 ± 0.27	0.3 ± 0.1	2.7	2020-10-29 7:01:24	VLASS	PySE
1278651	54.8335	−35.8063	0.6 ± 0.2	0.5 ± 0.1	2.7	2023-06-13 18:06:24	VLASS	PySE
1278651	54.8335	−35.8063	0.74 ± 0.71	0.5 ± 0.3	0.89	2019-04-27 5:54:00	RACS	PySE
1278651	54.8335	−35.8063	0.72 ± 0.7	0.5 ± 0.3	0.89	2019-04-28 3:14:00	RACS	PySE
1278651	54.8335	−35.8063	1.0 ± 0.3	1.0 ± 0.2	1.4	2020-12-31 13:34:27	RACS	PySE
1278651	54.8335	−35.8063	1.0 ± 0.3	0.9 ± 0.2	1.4	2021-01-07 13:25:42	RACS	PySE
1279472	53.7036	−35.6255	1.2 ± 0.3	1.1 ± 0.2	2.7	2020-10-29 7:01:24	VLASS	Catalog
1279472	53.7036	−35.6255	0.5 ± 0.4	0.4 ± 0.2	0.89	2019-04-27 5:54	RACS	PySE
1279472	53.7036	−35.6255	0.5 ± 0.4	0.4 ± 0.2	0.89	2019-04-28 3:14	RACS	PySE
1279472	53.7036	−35.6255	1.0 ± 0.3	0.9 ± 0.1	1.4	2020-12-31 13:34:27	RACS	PySE
1279472	53.7036	−35.6255	1.0 ± 0.3	0.9 ± 0.1	1.4	2020-12-31 13:51:12	RACS	PySE
1290071	224.7278	−59.5997	1.2 ± 0.3	1.2 ± 0.2	0.89	2019-05-07 12:41:05	RACS	PySE
1290071	224.7278	−59.5997	1.2 ± 0.3	1.2 ± 0.2	0.89	2019-05-07 13:27:32	RACS	PySE
1290071	224.7278	−59.5997	1.2 ± 0.3	1.2 ± 0.2	0.89	2020-05-02 15:48:10	RACS	PySE
1290071	224.7278	−59.5997	1.2 ± 0.3	1.2 ± 0.2	0.89	2020-06-19 13:35:51	RACS	PySE
1290071	224.7278	−59.5997	1.5 ± 0.3	1.5 ± 0.2	1.4	2021-03-14 20:49:38	RACS	PySE
1290071	224.7278	−59.5997	1.5 ± 0.3	1.5 ± 0.2	1.4	2021-03-15 18:54:55	RACS	PySE
1290071	224.7278	−59.5997	1.5 ± 0.3	1.5 ± 0.2	1.4	2022-03-04 19:17:23	RACS	PySE
1305970	48.3284	−52.7501	−0.1 ± 0.4	0.4 ± 1.0	0.89	2020-03-28 6:00	RACS	PySE
1305970	48.3284	−52.7501	−0.2 ± 0.4	0.1 ± 0.2	0.89	2020-03-28 6:17	RACS	PySE
1305970	48.3284	−52.7501	−0.1 ± 0.4	0.3 ± 0.5	0.89	2020-03-28 6:34	RACS	PySE
1305970	48.3284	−52.7501	0.3 ± 0.3	0.2 ± 0.1	1.4	2021-01-23 9:55:38	RACS	PySE
1305970	48.3284	−52.7501	0.3 ± 0.3	0.3 ± 0.1	1.4	2021-01-24 10:40:35	RACS	PySE
1308228	48.6663	−52.4636	0.1 ± 0.4	−0.6 ± 0.1	0.89	2020-03-28 6:00	RACS	PySE
1308228	48.6663	−52.4636	0.1 ± 0.4	−0.4 ± 0.8	0.89	2020-03-28 6:17	RACS	PySE
1308228	48.6663	−52.4636	0.1 ± 0.4	−0.4 ± 0.8	0.89	2020-03-28 6:34	RACS	PySE
1308228	48.6663	−52.4636	0.0 ± 0.3	8.0 ± 400	1.4	2021-01-23 9:55:38	RACS	PySE
1308228	48.6663	−52.4636	−0.1 ± 0.3	0.1 ± 0.2	1.4	2021-01-24 10:40:35	RACS	PySE
1318936	341.5495	−59.0375	0.4 ± 0.4	0.2 ± 0.1	0.89	2019-05-07 19:00	RACS	PySE
1318936	341.5495	−59.0375	0.4 ± 0.4	0.2 ± 0.1	0.89	2020-03-29 1:51	RACS	PySE
1318936	341.5495	−59.0375	0.3 ± 0.3	0.2 ± 0.1	1.4	2022-07-30 2:59:58	RACS	PySE

Note. Sources in italics are discussed in the text.

5.3. Interstellar Scintillation

Interstellar scintillation is a common cause of variability in the radio sky. M. A. Walker (1998) provides a review of the phenomenon with examples of its effects. Interstellar scintillation is caused by the radio waves from a distant, typically compact, object passing through the ionized component of the interstellar medium. This interaction causes a variation in the flux of the radio source characterized by the modulation index, m. The modulation index is defined by the fractional variation in the flux: $m = \sigma/\mu$, where σ is the variation in flux and μ is the average flux. This variability can be characterized over a particular timescale called the variability timescale, $t_{\rm var}$.

In order to predict the expected variability timescale and modulation index for a particular location on the sky, it is necessary to compare the observing frequency with the transition frequency, ν_0. At the transition frequency, the modulation index, or fractional variability, is expected to be at its highest, that is, of order unity. If the observing frequency is above the transition frequency, the scattering from the ionized interstellar medium is considered "weak"; if the observing frequency is below the transition frequency it is considered "strong." All of our observations occur in the "strong" scattering regime. Furthermore, within this regime, variability can be either from diffractive scintillation or from refractive scintillation. Diffractive scintillation occurs on narrow bandwidths and short timescales, while refractive scintillation occurs over longer timescales and over larger bandwidths. On the timescales and observing frequencies probed by our 30 minutes images, refractive scintillation is the most dominant type of scintillation.

Maps of the expected scintillation properties from the interstellar medium can be made if the distribution of charged particles is known. P. J. Hancock et al. (2019) use Hα intensity maps to generate a model of the electron content and distribution of our galaxy. From this model, the accompanying software also computes the expected transition frequency, variability timescale, and modulation index.

We use the software described by P. J. Hancock et al. (2019) to compute expected values of refractive scintillation at the pointing center of each field. A summary of the aforementioned scintillation parameters for each field is shown in Table 7. Several fields have very large modulation indices, which we can compare to V, the variability metric calculated for each source. All of the sources we consider variable are

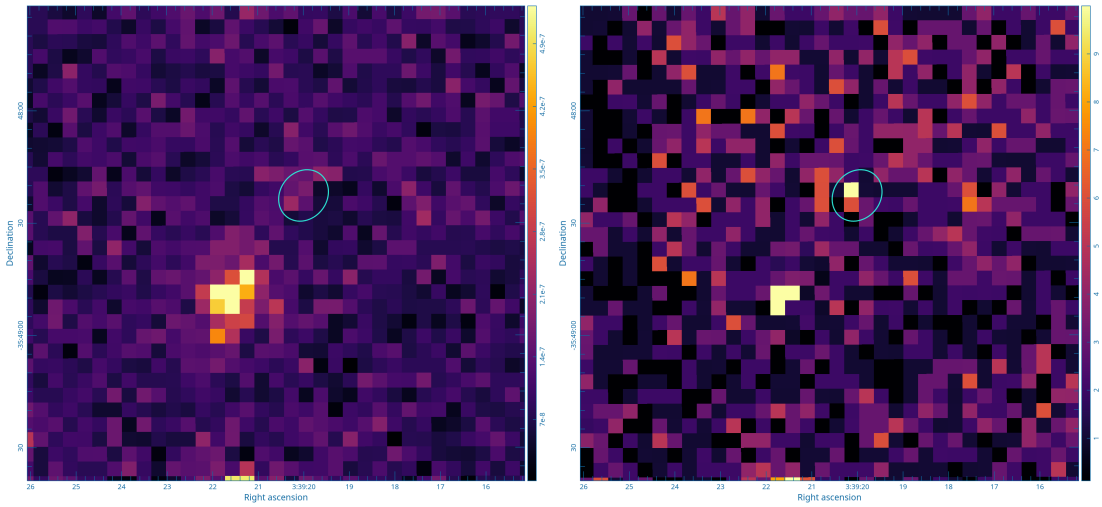

Figure 1. Left: a coadded image of Chandra ACIS data shown with the MeerKAT beam from one of the observations overplotted as an ellipse. Right: an image from Chandra ObsId 4175 in which the source appears to be detected.

shown in Table 8, with the variability statistics and an upper limit on the timescale of variation estimated by visual inspection of the light curves.

Comparing Tables 7 and 8 shows that all but one source can be considered consistent with refractive scintillation. The upper limit on the timescale of variation in source 1290071 is about half of the scintillation timescale expected with the variability parameter, V, being close to the modulation index, m. It could be that the assumed distance to the scattering screen used in the calculation of the scintillation characteristics is much less, perhaps half of the assumed 1.5 kpc. This change would result in the timescale matching the estimated upper limit of the variability timescale, with the modulation index being consistent as well. However, in Tables 5 and 6 we see that the radio measurements at 890 MHz of the RACS counterpart are quite stable. The stability of the flux in these measurements is interesting, although the observing cadence is not fine enough to rule out scintillation for this source.

Source 1278651 is only marginally detected in RACS at 1.4 GHz and is also only marginally detected in one of the VLASS epochs at 2.7 GHz. It is not detected in RACS at 890 MHz, which should have a sensitivity similar to RACS at 1.4 GHz, around 250 μJy. We can see from Table 7 that the modulation index for this source is quite high and the scintillation timescale is relatively short. Therefore these measurements from RACS and VLASS can still be reconciled with our measurements if this source is due to refractive scintillation.

5.4. Source 96178: A Highly Circularly Polarized Short Transient

As mentioned in Section 4.2, one source was confidently detected in the lower half of the MeerKAT L band with approximately 100% Stokes V polarization in the lowest frequencies on a timescale of 8–16 s. Given the nondetection in the upper half of the MeerKAT L band, the emission would need to either be narrowband or have a spectral index less than -1.4. One possible origin of emission of this kind is coherent emission from a stellar flare. It is shorter than typical stellar flares; however, due to the near-threshold detection this could be due to only capturing the very peak of the emission. Comparing this source to those of L. N. Driessen et al. (2024), the transient duration is significantly shorter than the duration of all of the observations included in the catalog. This transient is approximately 2″ away from a cataloged TESS M dwarf star that is 99 pc from Earth (TIC 419518448; K. G. Stassun et al. 2019). Both the TESS and MeerKAT light curves are shown in Figure 5. The TESS light-curve data are available at doi:10.17909/s4cr-6z50. These sources could be related, but the association is difficult to confirm without a better localization. It is possible that the slight bump in the TESS light curve could correspond to the MeerKAT transient, but the increase in flux is not very significant. Furthermore, the relatively coarse 10 minutes cadence is difficult to compare with the 8 s cadence of the MeerKAT light curve. There were no X-ray, gamma-ray or radio counterparts.

Another possible source type with high Stokes V polarization and a steep spectrum would be a pulsar. However, since this source is a transient source, the emission would have to be a giant pulse from a pulsar. There are no pulsars listed in the ATNF Pulsar Catalog (G. Hobbs et al. 2004) within a quarter of a degree of the source location, making such an origin unlikely. Compared to giant pulses from pulsars, coherent emission from a flare star is expected to be much more common (for a review, see R. A. Osten 2008). The timescale of the emission, potentially up to 16 s, also fits well with what would be expected from a flaring star compared to a pulsar, where, at L-band frequencies, the timescales would be expected to be much shorter. Another source type worth considering is the recently discovered LPRTs mentioned in Section 1. If this transient were a periodic source, the period would most likely be longer than 4 hr, the length of the observations. Such a period would be a bit long even for these LPRTs. Furthermore, these LPRTs are typically found in the Galactic plane, while this source is in an extragalactic field. It is nevertheless still a possibility given the low detection statistics at this time. Since this transient is likely a stellar flare, follow-up was not performed.

Table 7
Scintillation Properties at the Center of Each Field, Calculated Using the Software of P. J. Hancock et al. (2019)

Target	R.A. (deg)	Decl. (deg)	Modulation Index	Timescale (days)	ν_0 (GHz)
SN 2019muj	36.5771	−9.8359	0.69 ± 0.09	2.0 ± 0.8	2.5
SN 2020ue	190.6949	2.6595	0.53 ± 0.03	4.4 ± 0.6	3.9
SN 2020hvf	170.3602	3.0147	0.66 ± 0.07	2.3 ± 0.8	2.6
SN 2021smj	186.6940	8.8827	0.72 ± 0.11	1.7 ± 0.8	2.3
SN 2021qvv	187.0122	9.8056	0.71 ± 0.10	1.8 ± 0.7	2.3
SN 2022ffv	54.1238	−35.2893	0.56 ± 0.13	3.9 ± 2.7	3.6
SN 2020eyj	167.9466	29.3893	0.65 ± 0.07	2.3 ± 0.7	2.7
GRB 220730A	225.0143	−69.4959	0.29 ± 0.01	64.1 ± 9.5	11.5
GRB 200522A	5.6820	−0.2832	0.73 ± 0.12	1.7 ± 0.8	2.2
GRB 200907B	89.0290	6.9062	0.30 ± 0.01	59.9 ± 4.9	10.9
GRB 210919A	80.2545	1.3115	0.26 ± 0.01	64.5 ± 4.2	14.2
GRB 210726A	193.2909	19.1875	0.66 ± 0.07	2.2 ± 0.6	2.7
GRB 200411A	47.6641	−52.3176	0.91 ± 2.20	0.9 ± 6.7	1.5
GRB 210323A	317.9461	25.3699	0.37 ± 0.01	24.5 ± 2.4	7.5
GRB 200219A	342.6385	−59.1196	0.74 ± 0.65	1.7 ± 4.6	2.2
SN 2019np	157.3415	29.5107	0.66 ± 0.07	2.4 ± 0.8	2.7

Table 8
All Variable Sources in Our MeerKAT Survey with the Variability Statistics and the Estimated Timescale of Variability

Source	R.A. (deg)	Decl. (deg)	η	V	Timescale (days)	Modulation Index	Timescale (days)	ν_0 (GHz)
1252675	157.3791	29.8533	6.03	0.12	<58	0.66 ± 0.07	2.4 ± 0.8	2.7
1252803	157.2391	29.9353	4.92	0.40	<58	0.66 ± 0.07	2.4 ± 0.8	2.7
1260388	191.0687	2.3340	3.70	0.28	<17	0.53 ± 0.03	4.4 ± 0.6	3.9
1260578	190.8379	2.4131	2.53	0.21	<17	0.53 ± 0.03	4.4 ± 0.6	3.9
1266989	170.5800	2.8567	2.98	0.21	<7	0.66 ± 0.07	2.3 ± 0.8	2.6
1267266	170.4347	2.8388	3.19	0.18	<7	0.66 ± 0.07	2.3 ± 0.8	2.6
1267302	170.4211	3.3767	8.53	0.44	<7	0.66 ± 0.07	2.3 ± 0.8	2.6
1278651	54.8335	−35.8063	3.56	0.23	<13	0.56 ± 0.13	3.9 ± 2.7	3.6
1279472	53.7036	−35.6255	2.54	0.19	<0.8	0.56 ± 0.13	3.9 ± 2.7	3.6
1290071	224.7278	−69.5997	3.12	0.23	<29	0.29 ± 0.01	64.1 ± 9.5	11.5
1305970	48.3284	−52.7501	3.66	0.58	<0.02	0.91 ± 2.20	0.9 ± 6.7	1.5
1308228	48.6663	−52.4636	3.66	0.67	<0.02	0.91 ± 2.20	0.9 ± 6.7	1.5
1318936	341.5495	−59.0375	2.06	0.13	<0.06	0.74 ± 0.65	1.7 ± 4.6	2.2

Note. Sources in italics are discussed in the text.

5.5. Transient Rate Limits

Using the survey parameters along with the number of detected transients, which is zero on the longer timescales, we can place limits on the transient rate using the Radio Transients Simulations[12] (RATS; S. I. Chastain et al. 2022a). The details of the RATS code and how it computes the transient rate limits are described by S. I. Chastain et al. (2022b). In summary, the transient rates were computed by simulating transients, aggregating detection statistics, calculating transient rates for each field in the survey by using Poisson statistics, and taking an average over the transient rates weighted by the survey duration of each field and field of view.

Figure 6 shows the upper limit on transient rates calculated from RATS for the 30 minutes timescale using a simulated transient with a top-hat light curve, that is, a light curve that is essentially a step function. The left panel shows the simulated transient duration on the horizontal axis, the simulated transient peak flux on the vertical axis, and the upper limit to the transient rate on the color axis. In this plot, the darker colors show lower, more constraining upper limits. The red horizontal line marks 5 mJy. The right panel shows the profile of the upper limit to the transient rate as a function of transient duration for transients with a peak flux of 5 mJy. Our strictest limits show an upper limit of 10^{-4} transients per day per square degree for transients with a duration of about 200 days and flux of 5 mJy. Compared to the limits found by S. I. Chastain et al. (2023), this limit is approximately a factor of 2 lower at a similar transient duration. This may be due to this survey having a larger number of hours on target, 113 versus 100, or, perhaps more likely, having higher-quality images on average.

Figure 7 shows the transient rate calculated for the lower half of the L band at the 8 s timescale. This plot is similar to

[12] https://github.com/dentalfloss1/RaTS

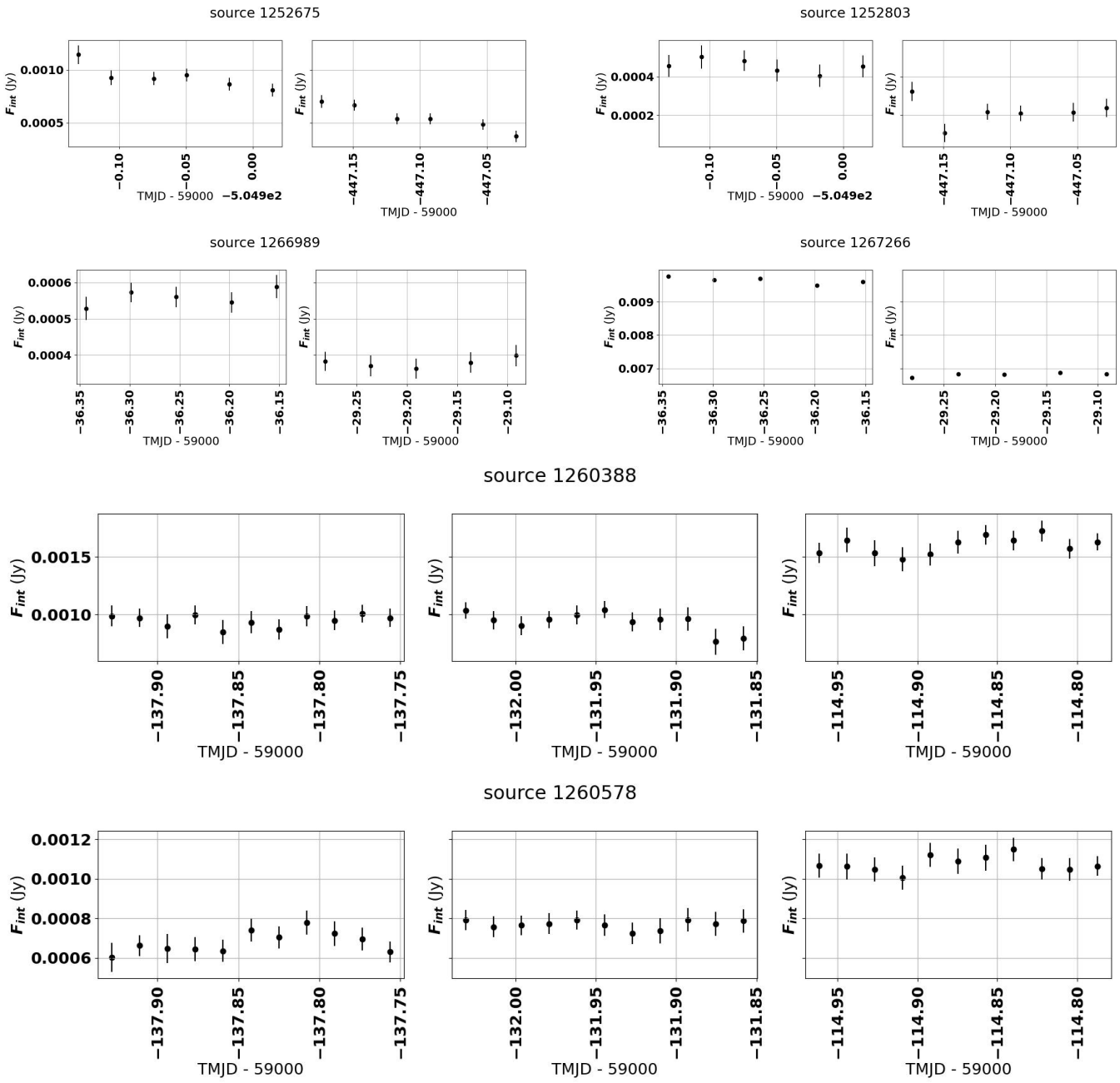

Figure 2. Light curves for the variable sources, not including source 1290071.

Figure 6, but with an additional plot showing the lower limits on the transient rate. The left panel shows the lower limit on the transient rate on the color axis, the middle panel shows the upper limit on the transient rate on the color axis, and the right panel shows the allowed values for the transient rate in the shaded region as a function of transient duration for a transient with a flux of 9.51 Jy. From the plot in the right panel, we can see that for a transient with a peak flux of 9.51 Jy and on timescales from 8 s down to milliseconds, we find a transient rate between 4×10^{-4} and 10^{-2} transients per day per square degree. These upper and lower limits are for this particular observing setup and highlight the importance of considering observing bandwidth when computing transient rates. The transient we saw was only visible when we split up the L band into two different subbands. Future updates to the transient rate simulations could include exploring the effects of observing bandwidth, transient spectral width, and dispersion on computations of transient rate. Such computations could inform future surveys about the optimal configuration for detecting steep-spectrum or narrowband sources.

6. Looking Forward

One of the remaining challenges for future radio surveys is accurately characterizing the transient rates or limits on the transient rates for the different kinds of transients that are being detected. The naive, straightforward approach is to simply count up the number of detections, take the timescale to

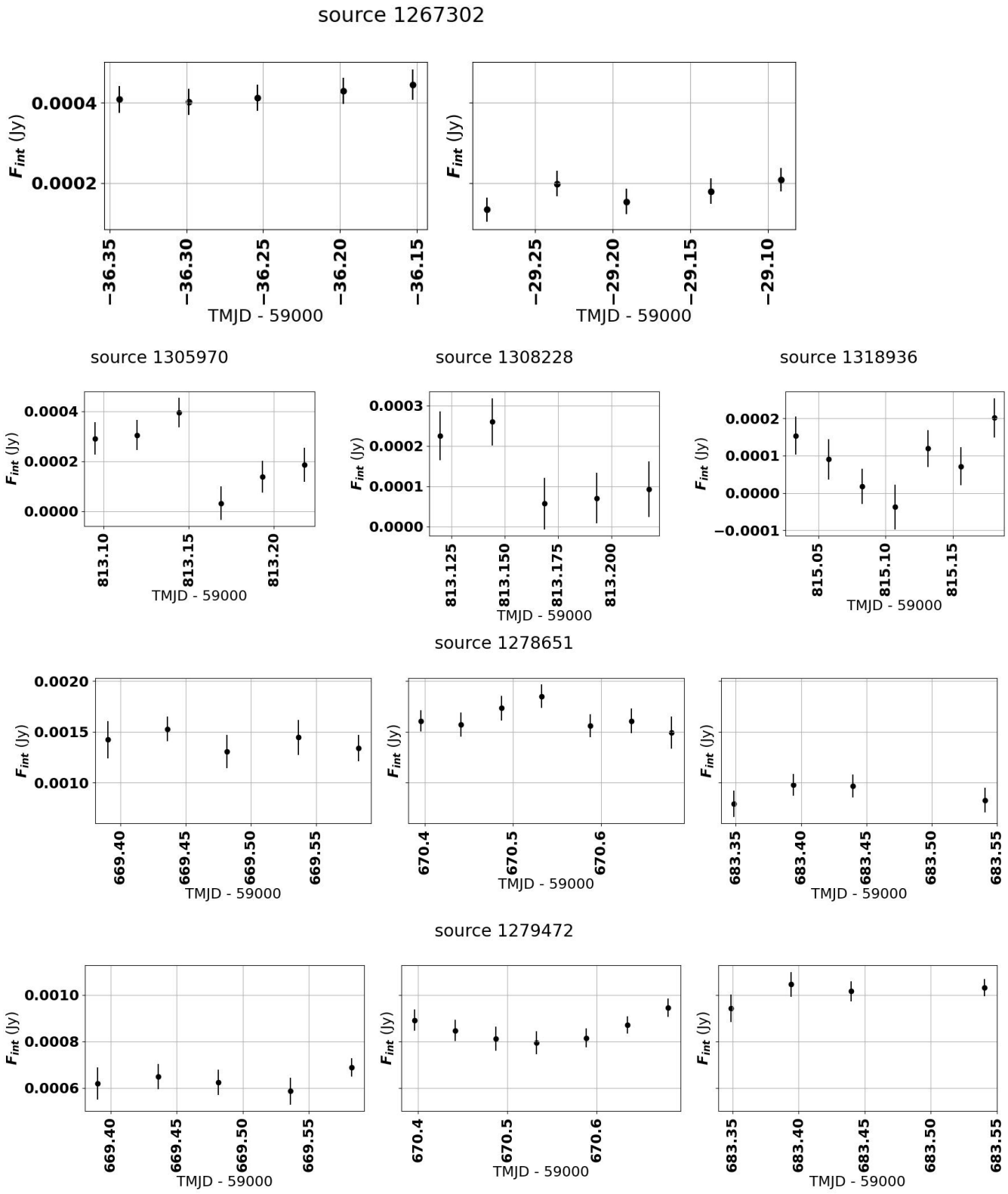

Figure 3. Light curves (continued) for the variable sources, not including source 1290071.

be the duration of the survey, then use a Poisson distribution to compute a simple transient rate. However, as discussed by D. Carbone et al. (2016, 2017) and S. I. Chastain et al. (2022b) this approach frequently produces results that are inaccurate representations of the transient rate due to effects such as transients falling in the gaps between observations and sensitivity varying between observations. Both S. I. Chastain et al. (2023) and this work attempt to more accurately compute

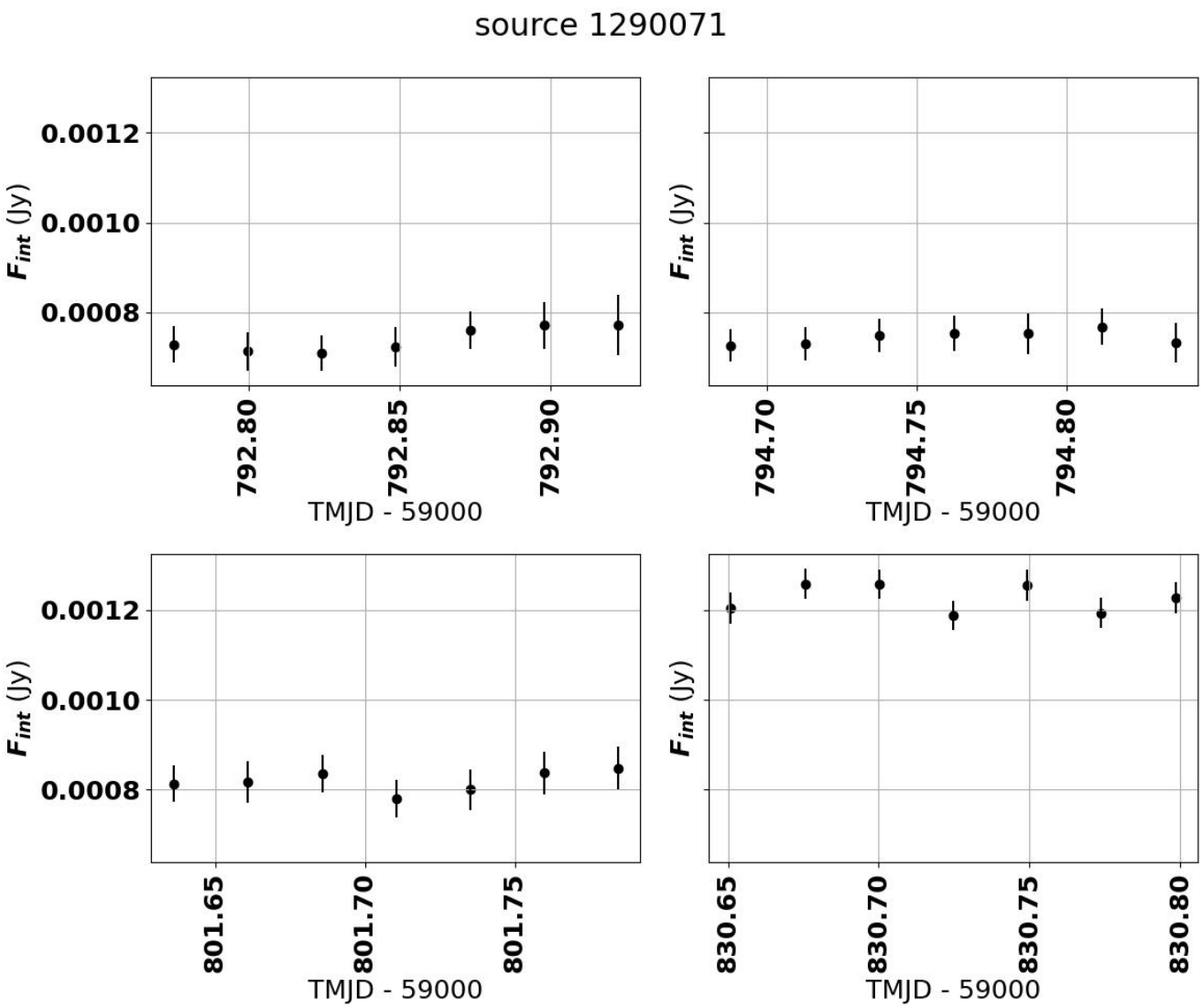

Figure 4. Light curve showing all observations of source number 1290071, which shows variability from one observation to the next. It also has radio counterparts, and the variability timescale of around 30 days does not match the refractive scintillation timescale of around 60 days.

the transient rate over a wide part of parameter space using the transient simulations described by S. I. Chastain et al. (2022b). In order to gain a meaningful understanding and comparison between the transient rates from different kinds of sources and surveys, current and future radio surveys will require more rigorous computation of the expected transient rates using techniques such as Monte Carlo simulations.

Another significant challenge is the large computational and time cost of performing a transient search such as the one described in this work. One contributing factor for the significant time cost was variability due to imperfect calibration of the images, including an imperfect primary beam shape that imparts artificial variability that can be seen in the source light curves. Another contributing factor was the choice to include images with elliptical beams. Future surveys with much larger data sets may choose to only select images with nearly circular beams and perhaps raise detection thresholds to avoid sidelobes from bright sources.

Addressing the large computational requirement may require new techniques for imaging the large amount of data in the survey. I. de Ruiter et al. (2024) describe a technique that accelerates the process by using sky model source subtraction to avoid the computationally intensive cleaning and primary beam correction process. For dense arrays, such as the MeerKAT core or the future DSA-2000, a GPU-based approach that does not perform any cleaning, such as that used by the Orville Wideband Imager on the Long Wavelength Array, could be appropriate. For details on this imager and some applications, see S. S. Varghese et al. (2021). If the challenges of computational and time cost can be overcome, this survey shows that searching for transients on an 8 s timescale could produce interesting results that otherwise would go undetected.

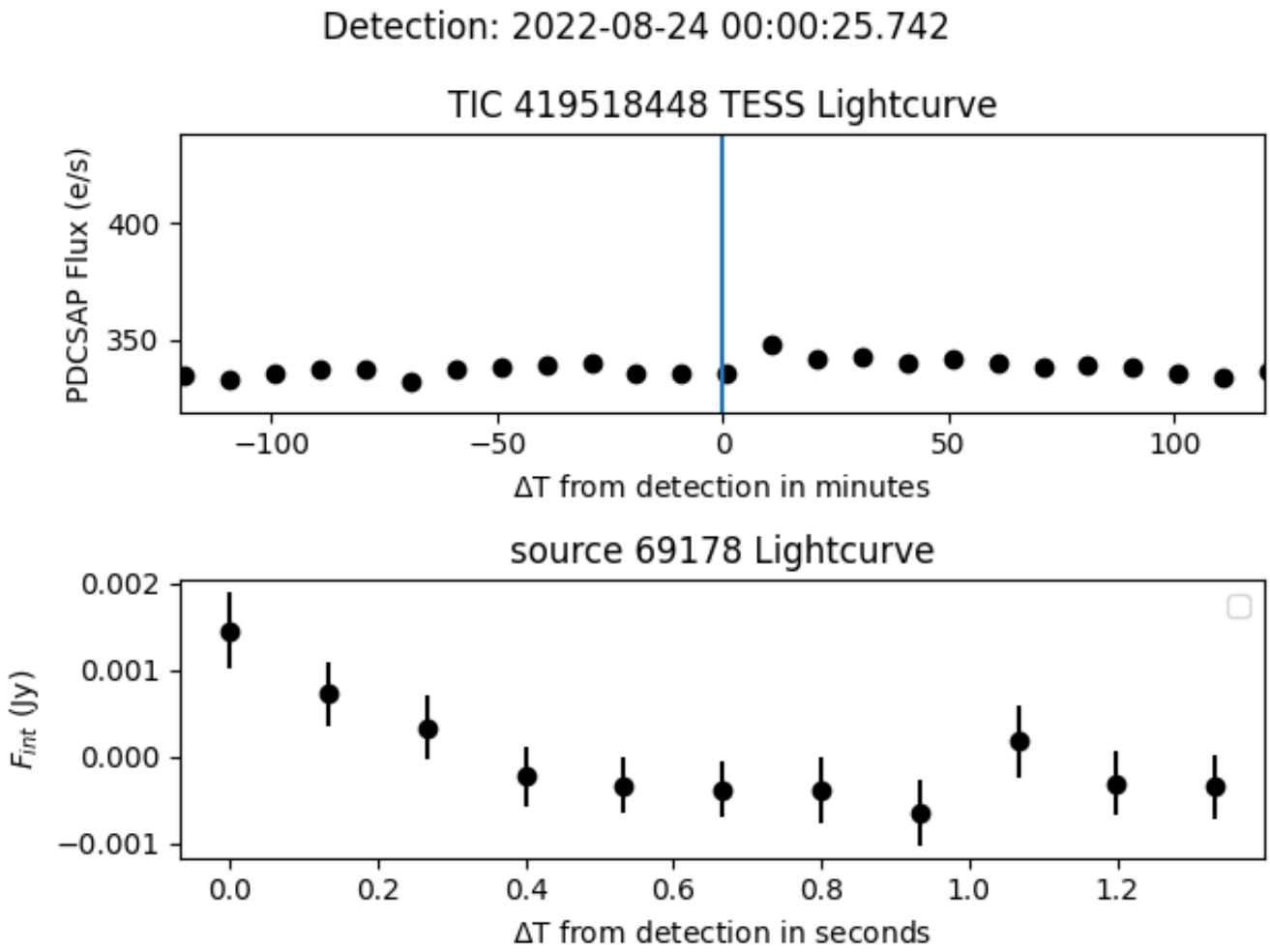

Figure 5. Top: the TESS light curve for TIC 419518448, a potential counterpart to source 96178. Bottom: the MeerKAT light curve.

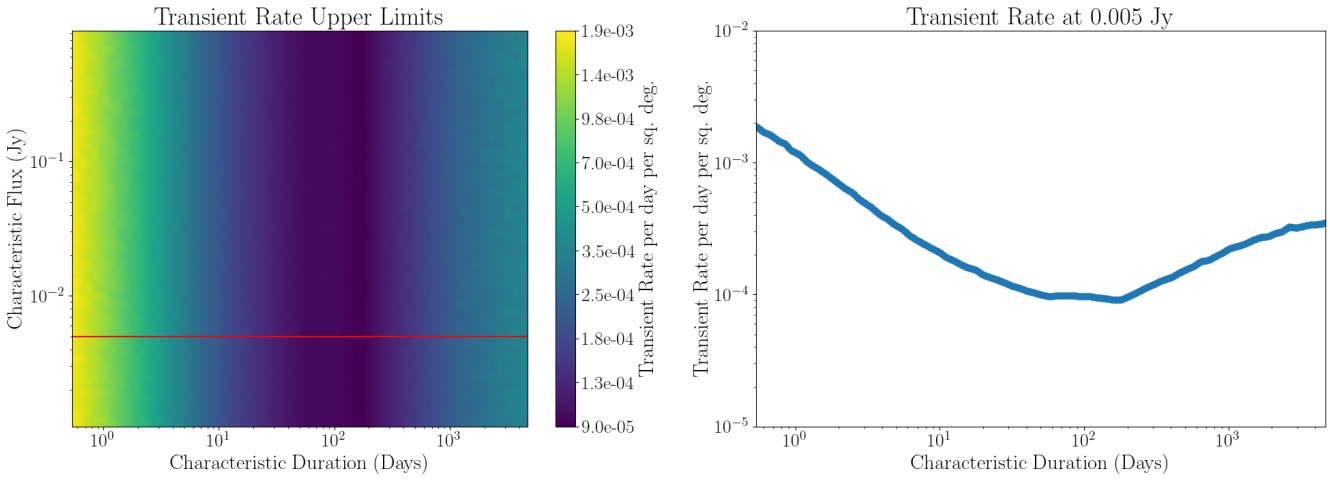

Figure 6. Left: a surface plot with the upper limit to the transient rate calculated for a top-hat light curve on the color axis, and the transient duration and peak flux on the horizontal and vertical axes, respectively. Right: the upper limit on the transient rate as a function of transient duration for transients with a peak flux of 5 mJy.

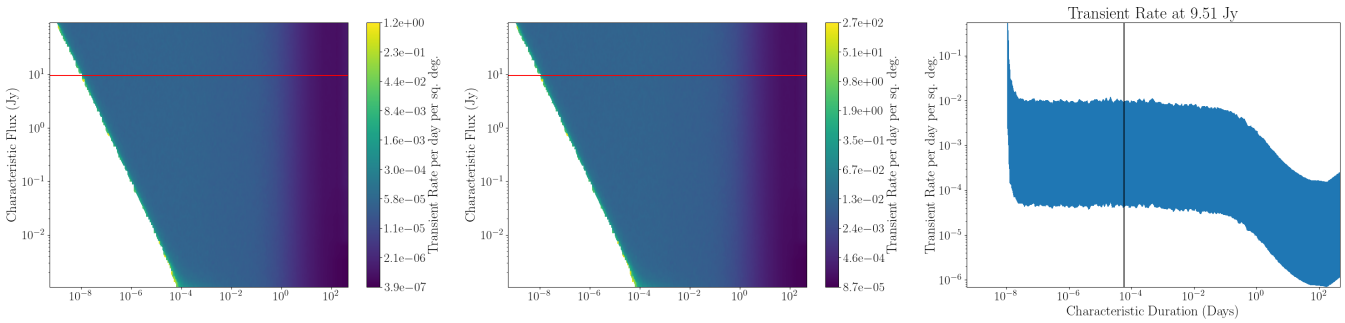

Figure 7. Left: a surface plot with the lower limit to the transient rate calculated for a top-hat light curve on the color axis, and the transient duration and peak flux on the horizontal and vertical axes, respectively. Middle: similar to the left panel, but showing the upper limits on the transient rate instead of the lower limits. Right: the lower and upper limits on the transient rate as a function of transient duration for transients with a peak flux of 9.51 Jy. A vertical line is plotted at a duration of 8 s.

7. Conclusion

We have conducted a commensal search on short GRB and SN fields using methodology developed by S. I. Chastain et al. (2023). In the 30 minutes images, we found 13 sources of astrophysical origin with statistically significant variability: sources 1252675, 1252803, 1260388, 1260578, 1266989, 1267266, 1267302, 1278651, 1279472, 1290071, 1305970, 1308228, and 1318936. We compared these sources with the RACS and VLASS surveys as well as catalog data from the Chandra space telescope. All but source 1290071 are consistent with interstellar scintillation. Many of the sources are likely AGNs, but one needs better localization to confirm its nature by matching the observations to optical and near-infrared observations. The variability of the remaining source could be intrinsic in nature. However, it could also be that the distance to the scattering screen used in calculating the expected refractive scintillation is about half of what is estimated.

On shorter, sub-minute timescales we found one possibly narrowband or steep-spectrum transient source with a duration around 8–16 s and a high degree of circular polarization in the lowest frequencies. This source is roughly consistent with a cataloged M dwarf star in the TESS Input Catalog (K. G. Stassun et al. 2019), but this association is difficult to confirm without a better localization. Since this source is likely to be a stellar flare, a dedicated follow-up campaign is not currently planned. However, this search does suggest that commensal searches like the current work could be a viable way of finding similar transients, especially if circular polarization is also examined. Finally, we place upper and lower limits on the transient rate using this survey, and find that the upper limit we place on the transient rate on longer timescales is a factor of 2 better than the commensal search presented by S. I. Chastain et al. (2023), likely due to more time spent on target and better overall quality of the images.

Acknowledgments

We would like to thank the referee for providing helpful feedback.

The MeerKAT telescope is operated by the South African Radio Astronomy Observatory (SARAO), which is a facility of the National Research Foundation, an agency of the Department of Science and Innovation. We would like to thank the operators, SARAO staff, and ThunderKAT Large Survey Project team.

This work was carried out using the data processing pipelines developed at the Inter-University Institute for Data Intensive Astronomy (IDIA) and available at https://idia-pipelines.github.io. IDIA is a partnership of the University of Cape Town, the University of Pretoria and the University of the Western Cape. We also acknowledge the computing resources provided on the High Performance Computing Cluster operated by Research Technology Services at the George Washington University.

This work made use of the CARTA (Cube Analysis and Rendering Tool for Astronomy) software (doi:10.5281/zenodo.3377984, https://cartavis.github.io).

This research has made use of the CIRADA cutout service at URL cutouts.cirada.ca, operated by the Canadian Initiative for Radio Astronomy Data Analysis (CIRADA). CIRADA is funded by a grant from the Canada Foundation for Innovation 2017 Innovation Fund (Project 35999), as well as by the Provinces of Ontario, British Columbia, Alberta, Manitoba and Quebec, in collaboration with the National Research Council of Canada, the US National Radio Astronomy Observatory and Australia's Commonwealth Scientific and Industrial Research Organization.

The ASKAP radio telescope is part of the Australia Telescope National Facility which is managed by Australia's national science agency, CSIRO. Operation of ASKAP is funded by the Australian Government with support from the National Collaborative Research Infrastructure Strategy. ASKAP uses the resources of the Pawsey Supercomputing Research Centre. Establishment of ASKAP, the Murchison Radio-astronomy Observatory and the Pawsey Supercomputing Research Centre are initiatives of the Australian Government, with support from the Government of Western Australia and the Science and Industry Endowment Fund. We acknowledge the Wajarri Yamatji people as the traditional owners of the Observatory site. This paper includes archived data obtained through the CSIRO ASKAP Science Data Archive, CASDA (https://data.csiro.au).

This research has made use of the VizieR catalog access tool, CDS, Strasbourg, France (doi:10.26093/cds/vizier). The original description of the VizieR service was published in F. Ochsenbein et al. (2000).

Some of the data presented in this paper were obtained from the Mikulski Archive for Space Telescopes (MAST) at the Space Telescope Science Institute. The specific observations analyzed can be accessed via doi:10.17909/s4cr-6z50. STScI is operated by the Association of Universities for Research in Astronomy,

Inc., under NASA contract NAS5–26555. Support to MAST for these data is provided by the NASA Office of Space Science via grant NAG5–7584 and by other grants and contracts.

This research has made use of software provided by the Chandra X-ray Center (CXC) in the application packages CIAO, ChIPS, and Sherpa.

A.H. is grateful for the support by the the United States–Israel Binational Science Foundation (BSF grant 2020203) and by the Sir Zelman Cowen Universities Fund. This research was supported by the Israel Science Foundation (grant No. 1679/23). This research was supported in part by grant NSF PHY-2309135 to the Kavli Institute for Theoretical Physics (KITP).

M.V. acknowledges financial support from the Inter-University Institute for Data Intensive Astronomy (IDIA), a partnership of the University of Cape Town, the University of Pretoria and the University of the Western Cape, and from the South African Department of Science and Innovation's National Research Foundation under the ISARP RADIO-MAP Joint Research Scheme (DSI-NRF grant No. 150551) and the CPRR HIPPO Project (DSI-NRF grant No. SRUG22031677).

Data Availability

Data are available upon request by email to sarchast@ttu.edu.

ORCID iDs

S. I. Chastain https://orcid.org/0000-0003-3507-335X
A. J. van der Horst https://orcid.org/0000-0001-9149-6707
A. Horesh https://orcid.org/0000-0002-5936-1156
A. Rowlinson https://orcid.org/0000-0002-1195-7022
M. Vaccari https://orcid.org/0000-0002-6748-0577
P. A. Woudt https://orcid.org/0000-0002-6896-1655

References

Anderson, M. M., Mooley, K. P., Hallinan, G., et al. 2020, ApJ, 903, 116
Anumarlapudi, A., Dobie, D., Kaplan, D. L., et al. 2024, ApJ, 974, 241
Bailer-Jones, C. A. L., Rybizki, J., Fouesneau, M., Demleitner, M., & Andrae, R. 2021, AJ, 161, 147
Caleb, M., Lenc, E., Kaplan, D. L., et al. 2024, NatAs, 8, 1159
Carbone, D., van der Horst, A. J., Wijers, R. A. M. J., & Rowlinson, A. 2017, MNRAS, 465, 4106
Carbone, D., van der Horst, A. J., Wijers, R. A. M. J., et al. 2016, MNRAS, 459, 3161
Chastain, S. I., van der Horst, A. J., Anderson, G. E., et al. 2024, MNRAS, 532, 2820
Chastain, S. I., van der Horst, A. J., & Carbone, D. 2022a, RTS: Radio Transient Simulations, Astrophysics Source Code Library, ascl:2204.007
Chastain, S. I., van der Horst, A. J., & Carbone, D. 2022b, A&C, 40, 100629
Chastain, S. I., van der Horst, A. J., Rowlinson, A., et al. 2023, MNRAS, 526, 1888
Collier, J. D., Frank, B., Sekhar, S., & Taylor, A. R. 2021, in XXXIVth General Assembly and Scientific Symp. Int. Union of Radio Science (URSI GASS) (Piscataway, NJ: IEEE), 14
Condon, J. J., Cotton, W. D., Greisen, E. W., et al. 1998, AJ, 115, 1693
de Ruiter, I., Meyers, Z. S., Rowlinson, A., et al. 2024, MNRAS, 531, 4805
de Ruiter, I., Rajwade, K. M., Bassa, C. G., et al. 2025, Natur, 9, 672
de Villiers, M. S., & Cotton, W. D. 2022, AJ, 163, 135
Dong, D. Z., & Hallinan, G. 2023, ApJ, 948, 119
Driessen, L. N., McDonald, I., Buckley, D. A. H., et al. 2020, MNRAS, 491, 560
Driessen, L. N., Pritchard, J., Murphy, T., et al. 2024, PASA, 41, e084
Driessen, L. N., Stappers, B. W., Tremou, E., et al. 2022, MNRAS, 512, 5037
Dykaar, H., Drout, M. R., Gaensler, B. M., et al. 2024, ApJ, 973, 104
Evans, I. N., Primini, F. A., Glotfelty, K. J., et al. 2010, ApJS, 189, 37
Fruscione, A., McDowell, J. C., Allen, G. E., et al. 2006, Proc. SPIE, 6270, 62701V
Garmire, G. P., Bautz, M. W., Ford, P. G., Nousek, J. A., & Ricker, G. R., Jr. 2003, Proc. SPIE, 4851, 28
Gordon, Y. A., Boyce, M. M., O'Dea, C. P., et al. 2021, ApJS, 255, 30
Hale, C. L., McConnell, D., Thomson, A. J. M., et al. 2021, PASA, 38, e058
Hancock, P. J., Charlton, E. G., Macquart, J.-P., & Hurley-Walker, N. 2019, arXiv:1907.08395
Helfand, D. J., White, R. L., & Becker, R. H. 2015, ApJ, 801, 26
Hobbs, G., Manchester, R., Teoh, A., & Hobbs, M. 2004, in IAU Symp. 218, Young Neutron Stars and Their Environments, ed. F. Camilo & B. M. Gaensler (Cambridge: Cambridge Univ. Press), 139
Hurley-Walker, N., McSweeney, S. J., Bahramian, A., et al. 2024, ApJL, 976, L21
Hurley-Walker, N., Rea, N., McSweeney, S. J., et al. 2023, Natur, 619, 487
Johnston, S., Taylor, R., Bailes, M., et al. 2008, ExA, 22, 151
Jonas, J. L. 2009, IEEEP, 97, 1522
Lacy, M., Baum, S. A., Chandler, C. J., et al. 2020, PASP, 132, 035001
Leung, J. K., Murphy, T., Ghirlanda, G., et al. 2021, MNRAS, 503, 1847
Liu, J. 2011, ApJS, 192, 10
McConnell, D., Hale, C. L., Lenc, E., et al. 2020, PASA, 37, e048
Metzger, B. D., Williams, P. K. G., & Berger, E. 2015, ApJ, 806, 224
Mooley, K. P., Hallinan, G., Bourke, S., et al. 2016, ApJ, 818, 105
Murphy, T., Kaplan, D. L., Stewart, A. J., et al. 2021, PASA, 38, e054
Ochsenbein, F., Bauer, P., & Marcout, J. 2000, A&AS, 143, 23
Osten, R. A. 2008, arXiv:0801.2573
Prusti, T., De Bruijne, J., Brown, A. G., et al. 2016, A&A, 595, A1
Ricker, G. R., Winn, J. N., Vanderspek, R., et al. 2015, JATIS, 1, 014003
Rowlinson, A., Meijn, J., Bright, J., et al. 2022, MNRAS, 517, 2894
Schroeder, G., Rhodes, L., Laskar, T., et al. 2024, ApJ, 970, 139
Shimwell, T. W., Röttgering, H. J. A., Best, P. N., et al. 2017, A&A, 598, A104
Somalwar, J. J., Ravi, V., Dong, D. Z., et al. 2025, ApJ, 982, 163
Somalwar, J. J., Ravi, V., & Lu, W. 2025, ApJ, 983, 159
Spreeuw, H., Swinbank, J., Molenaar, G., et al. 2018, PySE: Python Source Extractor for Radio Astronomical Images, Astrophysics Source Code Library, ascl:1805.026
Stassun, K. G., Oelkers, R. J., Paegert, M., et al. 2019, AJ, 158, 138
Stewart, A. J., Fender, R. P., Broderick, J. W., et al. 2016, MNRAS, 456, 2321
Swinbank, J. D., Staley, T. D., Molenaar, G. J., et al. 2015, A&C, 11, 25
The CASA TEAM, Bean, B., Bhatnagar, S., et al. 2022, PASP, 134, 114501
Tingay, S. J., Goeke, R., Bowman, J. D., et al. 2013, PASA, 30, e007
van Haarlem, M. P., Wise, M. W., Gunst, A. W., et al. 2013, A&A, 556, A2
Varghese, S. S., Dowell, J., Obenberger, K. S., Taylor, G. B., & Malins, J. 2021, JGRA, 126, e29296
Walker, M. A. 1998, MNRAS, 294, 307